Near-surface study at the Valhall oil field from ambient noise surface wave tomography

A. Mordret, M. Landès, N. M Shapiro, S. Singh, O. I Barkved, Philippe Roux

Geophysical Journal International

Geophys. J. Int. (2013) **193,** 1627–1643
Advance Access publication 2013 March 08

doi: 10.1093/gji/ggt061

Near-surface study at the Valhall oil field from ambient noise surface wave tomography

A. Mordret,[1] M. Landès,[1] N. M. Shapiro,[1] S. C. Singh,[1] P. Roux[2] and O. I. Barkved[3]

[1] *Institut de Physique du Globe de Paris, Sorbonne Paris Cité, CNRS (UMR* 7154*), Paris, France. E-mail: mordret@ipgp.fr*
[2] *Institut des Sciences de la Terre, Université Grenoble* 1, *CNRS UMR* 5275*, Grenoble, France*
[3] *BP, Stavanger, Norway*

Accepted 2013 February 11. Received 2013 February 7; in original form 2012 March 2

SUMMARY

We used 6 hr of continuous seismic noise records from 2320 four-component sensors of the Valhall 'Life of Field Seismic' network to compute cross-correlations (CCs) of ambient seismic noise. A beamforming analysis showed that at low frequencies (below 2 Hz) the seismic noise sources were spatially homogeneously distributed, whereas at higher frequencies (2–30 Hz), the dominant noise source was the oil platform at the centre of the network. Here, we performed an ambient noise surface wave tomography at frequencies below 2 Hz. We used vertical-component geophones CCs to extract and measure the Scholte waves group velocities dispersion curves that were then processed with a set of quality criteria and inverted to build group velocity maps of the Valhall area. Although Scholte wave group velocity depends on *S* wave, our group velocity maps show features similar to that was previously obtained from *P*-wave velocity full-waveform inversion of an active seismic data set. Since the dominant noise source at high frequency (above 3 Hz) was the oil platform, we determined a 2-D *S*-wave velocity model along a profile aligned with the platform by inverting group velocity dispersion curves of Love waves from transverse-component geophones CCs. We found that *S*-wave velocity down to 20 m was low and varied along the profile, and could be used to estimate *S*-wave static.

Key words: Interferometry; Interface waves; Seismic tomography; Europe.

1 INTRODUCTION

Surface wave tomography is one of the most common ways to study the Earth's superficial layers. The dispersion of surface waves allows us to investigate the subsurface shear waves velocity structure because the sensitivity of surface waves at depth depends on their frequencies with lower frequencies being sensitive to greater depth. Traditional global- and regional-scale surface wave tomographies are based on records from earthquakes (e.g. Trampert & Woodhouse 1995, 2003; Ritzwoller & Levshin 1998; Ritzwoller *et al.* 2001; Shapiro & Ritzwoller 2002; Ekström 2011). As a consequence, their resolution strongly depends on the spatial and temporal distribution of seismicity and seismic stations.

A major development in the surface wave tomography was the recent use of cross-correlations (CCs) of ambient seismic noise to reconstruct Green's functions (GF) between pairs of stations. It has been shown theoretically that the GF between different receiver locations can be retrieved from the CC of sufficiently long recordings of a random wavefield for any inhomogeneous medium (e.g. Weaver & Lobkis 2001; Wapenaar 2004; Gouédard *et al.* 2008). This method was first used in helioseismology by Duvall *et al.* (1993) to retrieve acoustic waves propagating within the Sun. A seminal acoustic experience by Weaver & Lobkis (2001) brought a strong evidence that this method was viable for elastodynamic applications. Shapiro & Campillo (2004) were the first to show the reconstruction of the surface wave part of the GF between seismometers spread over the United States from the CC of long seismic noise time-series. The dispersion curves for surface waves extracted from the correlation functions (CCs) were similar to those retrieved from earthquakes. Therefore, one can apply conventional surface wave tomography techniques to these measurements to produce group velocity maps of regions with dense seismic station coverage. After first application of ambient noise seismic tomography by Sabra *et al.* (2005) and Shapiro *et al.* (2005) for California, the method has been widely used for continental- or regional-scale studies of the crust and the uppermost mantle (e.g. Lin *et al.* 2007, 2008; Moschetti *et al.* 2007; Yang *et al.* 2007; Zheng *et al.* 2008; Stehly *et al.* 2009). It has also been applied to image volcanic edifices (Brenguier *et al.* 2007) on small scale. However, ambient noise tomography has been traditionally undertaken in continental context and there are only few studies in oceanic environment, mainly because of the limited availability of seismic networks on the ocean bottom and of the short time during which they are deployed. Nonetheless, Stewart (2006) was the first to show the possibility of retrieving the GFs between ocean bottom

stations and Lin *et al.* (2006) have shown the possibility of seismic noise correlation between island/island and island/continent station pairs. Harmon *et al.* (2007) have used the correlations between 10 broad-band ocean bottom seismometers to study the shallow structure of the young oceanic lithosphere. They inferred the average crustal and upper-mantle shear velocity structure of an area in the central Pacific Ocean, near the East Pacific Rise. Recently, Yao *et al.* (2011) undertook a similar study with more sensors in the Quebrada/Discovery/Gofar transform faults region on the East Pacific Rise.

The distribution of noise sources strongly controls the quality of the GFs. Most of seismic noise sources are superficial and result for instance from the interaction between the oceans, the atmosphere or the human activities with the solid Earth. As a consequence, the fundamental mode of surface waves is more easily extracted from noise correlations (Kimman & Trampert 2010). However, heterogeneous azimuthal distribution of sources may result in preferential GFs reconstruction (Stehly *et al.* 2006), one need to have enough seismic noise sources aligned with a particular station pair to sufficiently illuminate the wave propagation path between these sensors (e.g. Snieder 2004). The distribution of seismic noise sources also strongly depends on the frequency range: oceanic microseisms (0.03–1 Hz) used in most of regional-scale noise tomographies are generated by a non-linear interaction between oceans and solid Earth (Longuet-Higgins 1950) and their sources are distributed over the whole globe providing a good azimuthal coverage when correlating time-series that are more than 1 yr in duration (Yang & Ritzwoller 2008). At higher frequencies, the dominant seismic noise sources are often related to the human activity. In such situations, a study of particular source distribution is required before using CCs for imaging.

The data from industrial seismic networks with a large number of sensors may bring new possibilities for using noise correlations to study the shallow subsurface. Bussat & Kugler (2011) and de Ridder & Dellinger (2011) were the first to demonstrate the feasibility of noise-based imaging from dense ocean bottom recording networks for industrial applications. In this work, we use continuous seismic noise records from the 'Life of Field Seismic' network (*LoFS*, Fig. 1) to study the structure of the seabed at the Valhall oil field. We aim to demonstrate the applicability of the noise-based imaging for a wide frequency range from the ocean bottom cable (OBC) data.

The Valhall oil field is situated at the far southern end of the Norwegian North Sea at a 70-m water depth; the reservoir top is located around 2400 m below sea level. This oil field was discovered in 1975 and started production in 1982 and is currently operated by BP Norge A/S with a daily production of about 100 000 barrels of light oil. The production is expected to continue until 2048 (van Gestel *et al.* 2008). At first, the recovery rate was 14 per cent but technological breakthrough and an aggressive reservoir management increased this rate to 40 per cent (Barkved *et al.* 2003). In 2003, BP installed a permanent network of ocean bottom cable, called 'Life of Field Seismic' which was the world's largest permanent seismic array on the ocean bottom at that time. The network covers 70 per cent of the field area and consists of 120 km of ocean bottom cables buried 1 m depth in the soil where data are continuously recorded by 2320 four-component seismic sensors (4C: Z-vertical, N-north, E-east components and H-hydrophone) (e.g. van Gestel *et al.* 2008).

In a first part of this paper (Section 2), we present the data and the pre-processing to compute the CC. In Section 3, we determine the distribution of seismic noise sources around the *LoFS* network as a function of the frequency using a subset of the ∼30 million possible CCs. In Section 4, we describe the methods used to extract dispersion curves from CCs as well as the tomography formalism applied for our inversions. We present tomography results across the whole *LoFS* network at frequencies around 1 Hz. In Section 5, we show the possibility to perform a 2-D tomography at high frequency along a vertical profile using pairs of stations suitably aligned with the dominant noise source.

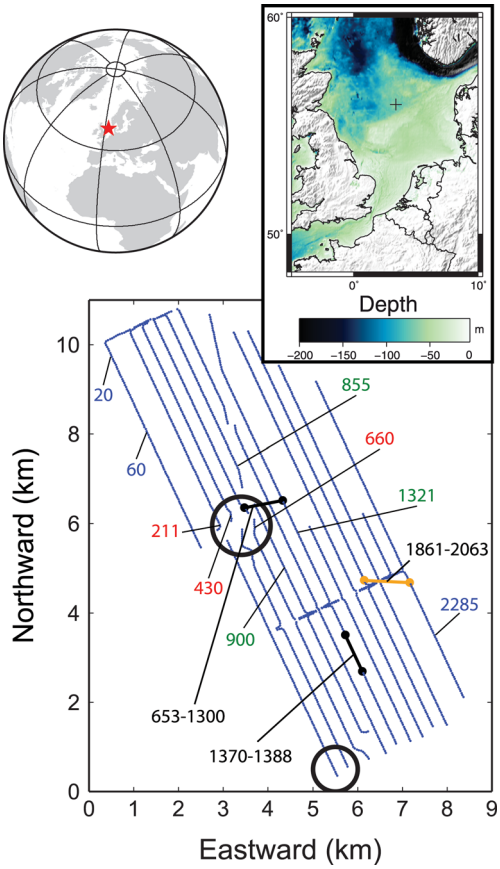

Figure 1. Map of the Valhall *LoFS* array. Each blue point represents a 4C sensor. The black circles show the approximate positions of the exploitation platforms. The coloured numbers refer to the stations used in Fig. 2. The bold black lines and points are the station pairs used in Fig. 3. The bold orange line and points are the station pair used in Fig. 8. The insets show the geographical location of the Valhall field with the black cross showing the location of the Valhall *LoFS* array. The bathymetry is shown as the background of the right inset.

2 NOISE CCs FROM THE *LoFS* NETWORK

2.1 The raw data

We analysed 400 min of continuous records from 2320 4C seismic sensors, sampled at 250 Hz. The data were recorded with a low-cut filter that removed most of the energy below 0.4 Hz. Because of the presence of the exploitation platform in the centre of the array, the amplitude and frequency content of the records vary with the position of the sensors. Fig. 2(a) shows examples of 400-min vertical components records filtered between 0.4 and 2 Hz (station #211, #855 and #20, Fig. 1). We see a drastic increase in amplitude as one gets closer to the oil platform. Fig. 2(b) shows amplitude spectra from nine stations (#20, #60, #211, #430, #660, #855, #900,

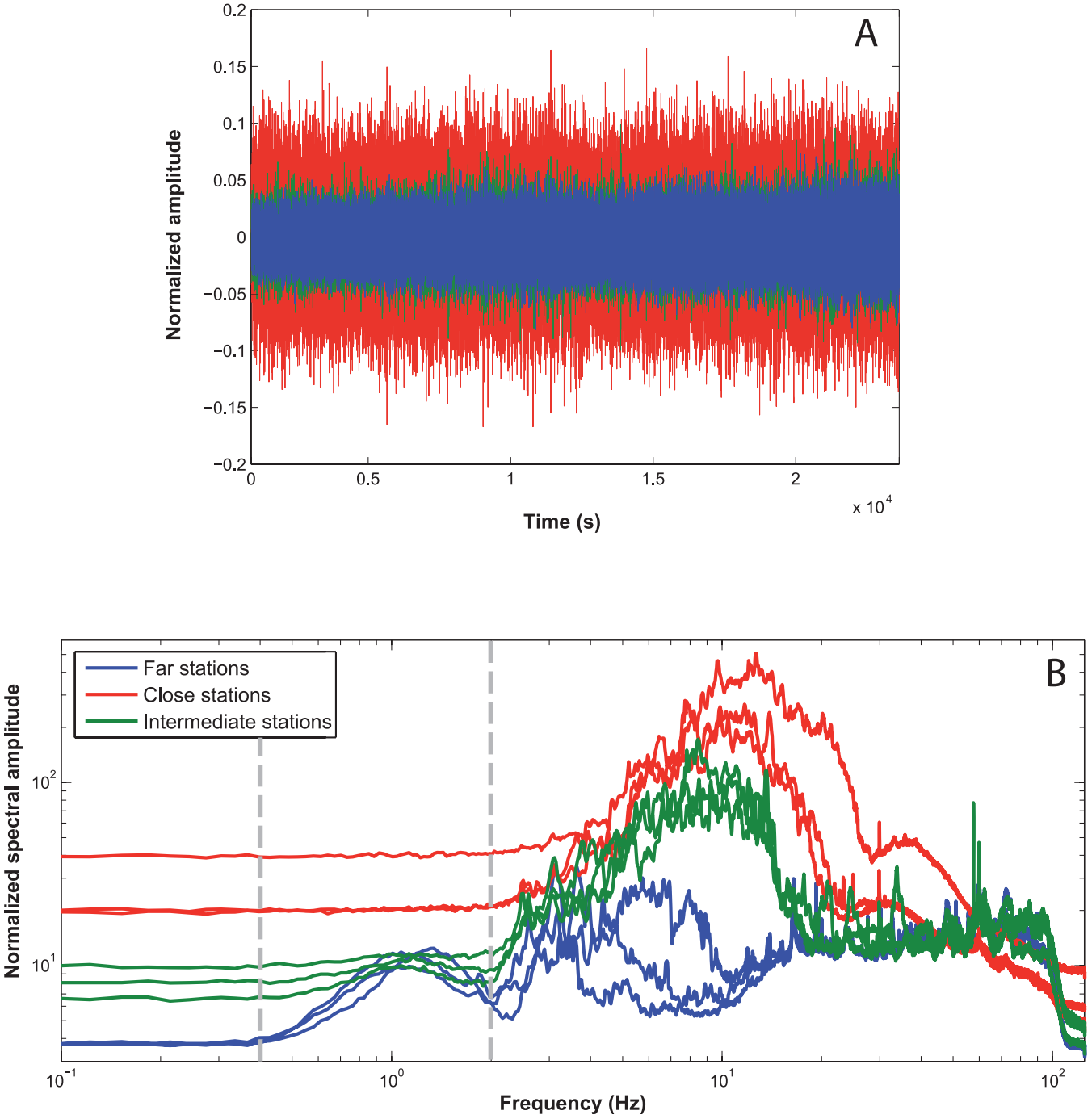

Figure 2. (a) Continuous records from three stations (211, 855, 20; see Fig. 1 for locations). The blue signal is from a station far from the platform, the green at an intermediate distance and the red close to the platform. (b) Averaged amplitude spectra of records at different stations. The blue curves are spectra from three stations away from the platform, the green curves are spectra from three stations at intermediate distance from the platform and the red curves are spectra from stations close to the platform. The light grey dashed lines denote the frequency band used for the Scholte wave tomography.

#1321 and #2285, Fig. 1) that were computed from 1-min long segments of record and averaged over the 400 min total duration of the data set. Again, we observe an overall increase of the noise amplitude as one goes closer to the platform as well as a shift of the main peak towards the higher frequency. This pattern is mainly due to the attenuation of high-frequency noise produced by the platform as it propagates in the subsurface away from the source. In the vicinity of the platform, the tail of the secondary microseismic peak around 1 Hz is progressively overwhelmed by the platform-generated noise. The reconstruction of GFs from noise CCs is problematic in the areas dominated by the localized noise sources, which will be discussed in the sections below.

2.2 Pre-processing the data and computing CCs

We organize the data in 400 1-min duration segments. The signal pre-processing is done station by station and segment by segment

and includes: (1) removal of the mean and the trend of the signal, (2) whitening of the amplitude spectrum between 0.4 and 30 Hz, (3) one-bit normalization of the traces (e.g. Bensen *et al.* 2007). We do not remove the instrumental response because all sensors were identical. Finally, we correlate each 400 sections for every interstation and intercomponent combinations and the resulting 400 correlations for each combination are stacked. We computed 10 intercomponent combinations: the nine components corresponding to the elastic Green's tensor (ZZ, ZE, ZN, EZ, EE, EN, NZ, NE and NN, with Z-vertical, N-north and E-east components) and the Hydrophone–Hydrophone (HH) component. We did not compute the Hydrophone–Geophone components to avoid dealing with different instrumental responses. At the end, we obtained 26 900 400 correlations, that is 2 690 040 correlations per intercomponent combination. The full analysis of this enormous amount of data is out of the scope of this study. In this paper, we only present an analysis of a subset of the computed CCs.

A quick overview of the data shows that there is a strong difference between the ZZ CCs computed from station pairs close to the platform (Fig. 3b, hereafter called near-platform CCs) and those computed from station pairs away from the platform (hereafter called distant CCs, Fig. 3a). On the distant ZZ CCs, we can see an acoustic wave (in green in Fig. 3a) with frequency >20 Hz. In the example shown in Fig. 3(a), the CC has an interstation distance of 896 m, the acoustic wave arrival time is around 0.6 s that makes an apparent velocity around 1500 m s^{-1}. As shown by the inset in Fig. 3, this acoustic wave is also present on the HH CC, with the same arrival time. It is followed by a lower frequency interface wave (between 5 and 20 Hz, yellow in Figs 3a–c) and with a velocity of 300–400 m s^{-1}. These two waves are clearly visible at both positive and negative lag times. However, amplitudes of these waves on both sides of CCs are not equal. Near-platform ZZ CCs exhibit a single long wave train emerging from the noise that clearly is not symmetric (red in Figs 3b and d). The interstation distances are similar for both examples in Fig. 3 to emphasize the differences between the near-platform CCs and the distant CCs. Overall, the recovered CCs are dominated by waves propagating in the water and in the solid near-surface layers. Their asymmetric character is explained by the inhomogeneous distribution of the noise sources.

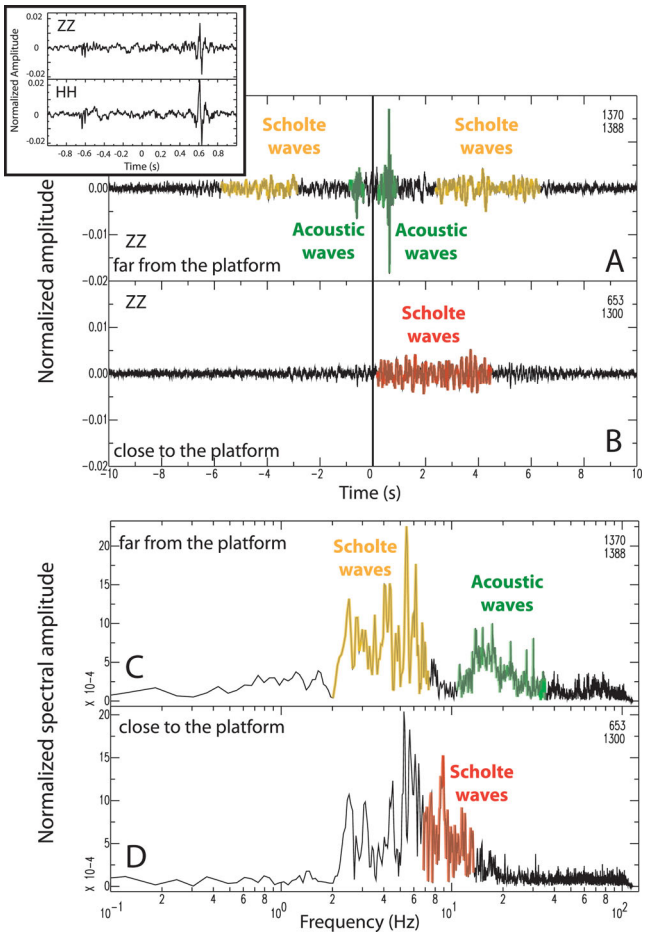

Figure 3. Examples of vertical-to-vertical (ZZ) noise cross-correaltions (CCs) (a and b) and corresponding amplitude spectra (c and d). (a) and (c) ZZ CC and corresponding spectrum for station pair 1370–1388 (Fig. 1) at interstation distance of 896 m. In the inset, at the top, a zoom of the ZZ correlation for times of −1 to 1 s showing in detail the acoustic wave. In the inset, at the bottom, we show the same zoomed part of the Hydrophone–Hydrophone correlation for comparison. (b and d) idem (a and c) for station pair 653–1300 at interstation distance of 855 m. Acoustic waves are indicated in green lines, Scholte waves in yellow for the distant CC (a) and in red for the near-platform CC (b). Amplitude spectra are computed from parts of CCs between −7 and 7 s.

3 DISTRIBUTION OF COHERENT SEISMIC NOISE SOURCES

Traveltime measured from noise CCs may be biased in a case of a strongly inhomogeneous distribution of noise sources (e.g. Campillo *et al.* 2011). Therefore, we first analyse the computed CCs with a goal to better characterize the location of the coherent noise sources and the type of waves in the CCs.

3.1 Beamforming analysis of the noise correlations of the wavefield recorded by the *LoFS* array

We carry out a beamforming analysis (e.g. Rost & Thomas 2002) to vertical-to-vertical CCs to determine the directions and the apparent velocities of the different waves present in the noise CCs, that is, the coherent noise wavefield recorded at Valhall and averaged over the whole 6-hr period (e.g. Roux 2009; Landès *et al.* 2010).

We use a plane wave beamforming technique that assumes that the waves in the CCs are plane waves coming from the direction of the source-side station. The waveform traveltimes are aligned to specific values of slowness and azimuth and then stacked. The energy of the stacked signal is expected to maximize at values corresponding to the incoming wave parameters. The main difficulty in applying this method to the *LoFS* network is the alignment of recorders along the ocean bottom cables that results in a strongly dominating azimuth (155°–335°) which biases the beamforming result. Another strong source of beamforming artefacts is the dominant interstation distances of ∼50 m inline and ∼300 m crossline. Therefore, to obtain a satisfactory distribution of stations, we selected a subarray (hereafter called SR5, in yellow on Fig. 4). The insets in Fig. 4 show the distance distribution and azimuthal coverage of the SR5 array. We see that there is still a strong domination of the 155° azimuth even if the distance range is more homogeneous. Thus, we decided to introduce an additional weighting scheme to compensate contributions from dominating azimuths.

We consider an N-sensor array where (x_i, y_i) are the coordinates of the sensors. For a plane wave propagating with a slowness vector $\mathbf{s}(s_x, s_y)$, the delay at station $\mathbf{i}$ will be $\mathbf{s}.\mathbf{r_i}$ where $\mathbf{r_i}$ is the position relative to the reference station. In the frequency domain, this delay

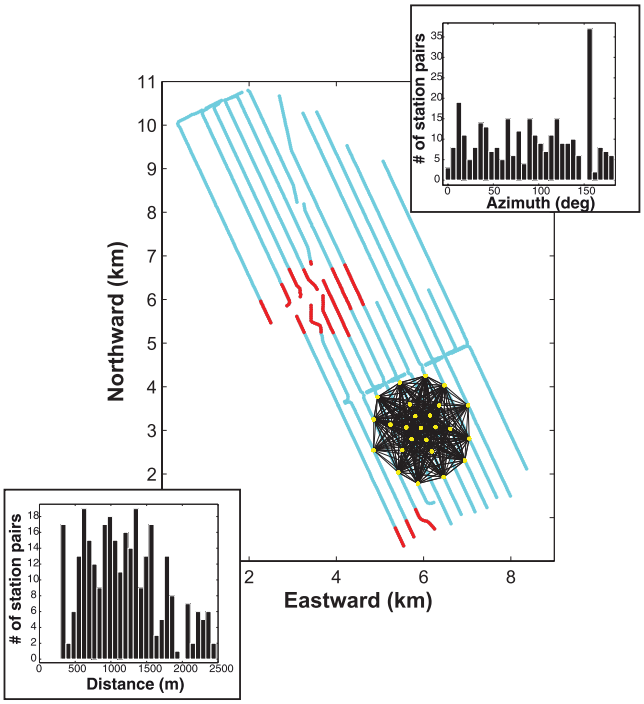

Figure 4. Map of the SR5 subarray used for the beamforming (yellow points). Red dots show the stations contaminated by the platforms noise. The top inset shows the azimuthal distribution of the station pairs in the SR5 array. Note that the preferred azimuth of the cables (155°) is still visible. The bottom inset shows the distribution of the distance between sensors in the SR5 array.

is equivalent to a phase shift $e^{-i\omega(\mathbf{s}.\mathbf{r_i})}$, for which the intensity of the targeted CC is expected to sum coherently. Finally, we perform a grid search over the slowness plane and compute at every position $\mathbf{s}(s_x, s_y)$ the amplitude of the stacked signal

$$B(s_x, s_y) = \frac{1}{N(N-1)\Delta T} \times \int_{-\Delta T}^{\Delta T} \left| IFT\left(\sum_{i,j=1,2}^{N-1,N} W_{ij} C_{ij}^a(\omega) e^{-i\omega(\mathbf{s}.\mathbf{r_{i,j}})} \right) \right| \mathrm{d}t, \quad (1)$$

where C_{ij}^a is the analytic signal of the CCs defined in the frequency domain as $C_{ij}^a(\omega) = C_{ij}(\omega)(1 + sgn(\omega))$ where C_{ij} are the Fourier transform CCs computed between stations i and j. The CCs are filtered in different frequency bands prior the beamforming and we associate a weight $W_{ij} = |\mathbf{r_{i,j}}|/n_{ij}$ to each of them, where $\mathbf{r_{i,j}}$ is the distance between station i and i, n_{ij} being the number of pairs of stations that have a similar azimuth and $|\mathbf{x}|$ the modulus of $\mathbf{x}$. This weight limits the influence of the preferential azimuth due to the cable geometry. IFT denotes the inverse Fourier transform. We set up the time window ΔT to fit with the length of the dominant signal on the CCs (typically ΔT is about one period) to avoid integrating noise in the beamforming output.

Fig. 5 shows results in two frequency bands: 0.4–2 Hz and 10–30 Hz bands. At frequencies below 2 Hz, where the coherent noise is dominated by the tail of the secondary microseismic peak (e.g. Webb 1998) the sources are relatively homogeneously distributed over all azimuths and the average phase velocity of incoming waves is ∼400–500 m s^{-1} (Fig. 5a). This result indicates that at these relatively low frequencies the coherent noise contains enough Scholte waves with spatially equidistributed sources that can be used for the noise-based tomography (Fig. 5c).

On the other hand, the higher frequency coherent noise (10–30 Hz) is mainly made of acoustic waves with energy arriving at 1500 m s^{-1} (Figs 5b–d). The beamforming analysis suggests that the platform is the dominant noise source in this frequency band.

3.2 Locating noise sources at intermediate frequencies

At intermediate frequencies (2–10 Hz), the noise correlations are dominated by strongly dispersive surface waves (Fig. 6a) on both vertical and transverse components that are sensitive to local shallow subsurface structure (e.g. Muyzert *et al.* 2002; Dellinger & Yu 2009; Landès *et al.* 2009). For instance, Fig. 6(a) shows that the lowpass filtered (10 Hz) vertical-to-vertical CCs for pairs of stations separated by 500 m, located on the profile AB exhibit a sinus-like moveout along the profile suggesting the presence of a localized source. To go beyond the beamforming, we used a different approach to locate the main source of the noise in this frequency range. In the case of a single localized noise source, the traveltimes of the main arrivals seen in CCs are related to the orientation and distance of the considered pairs of receivers relative to the source position (Shapiro *et al.* 2006). We took a sample of 1000 randomly chosen receiver pairs with interstation distances less than 2 km and measured arrival times ΔT_i of the maxima of the envelopes from the corresponding CCs filtered between 2 and 10 Hz. We then define the following misfit function:

$$S(r_S, V) = \sum_i \left| \frac{dist(B_i, r_S) - dist(A_i, r_S)}{V} - \Delta T_i \right|, \quad (2)$$

where $dist(x, y)$ is the distance between x and y, r_S is the position of the source, V is the group velocity and index i corresponds to pairs of stations with stations A_i and B_i. We use a grid search to minimize $S(r_S, V)$ and to find the optimal source position and the average group velocity.

We tested different randomly selected subsets of station pairs that showed that source position and group velocity estimations are very robust. Results for one of these realizations for Love waves are presented in Figs 6(b) and (c) that clearly shows that the coherent transverse-component noise at frequencies between 2 and 10 Hz is mainly generated by the drilling platform and that the average group velocity of Love wave at these frequencies is close to 320 m s^{-1}. We performed the same analysis for Scholte waves on vertical–vertical component CCs and we found the same source location and an average group velocity of 250 m s^{-1} (see Supporting Information, Fig. S1).

Overall, we observe two types of wave in the ZZ CCs, with two distinct sources in three distinct frequency bands. First, at low frequency (0.4–2 Hz), we see relatively homogeneously distributed sources of Scholte waves that come from the secondary microseism. Secondly, at intermediate frequency (2–10 Hz), we see Scholte (and Love) waves produced by the platform. And thirdly, at high frequency (10–30 Hz), we observe acoustic waves, still produced by the platform.

4 SURFACE WAVE TOMOGRAPHY

The presence of a high-frequency localized source requires separate analyses of low- and high-frequency signals. At frequencies below 2 Hz, where the noise is mainly composed of Scholte waves with a nearly homogeneous azimuthal distribution, we performed a

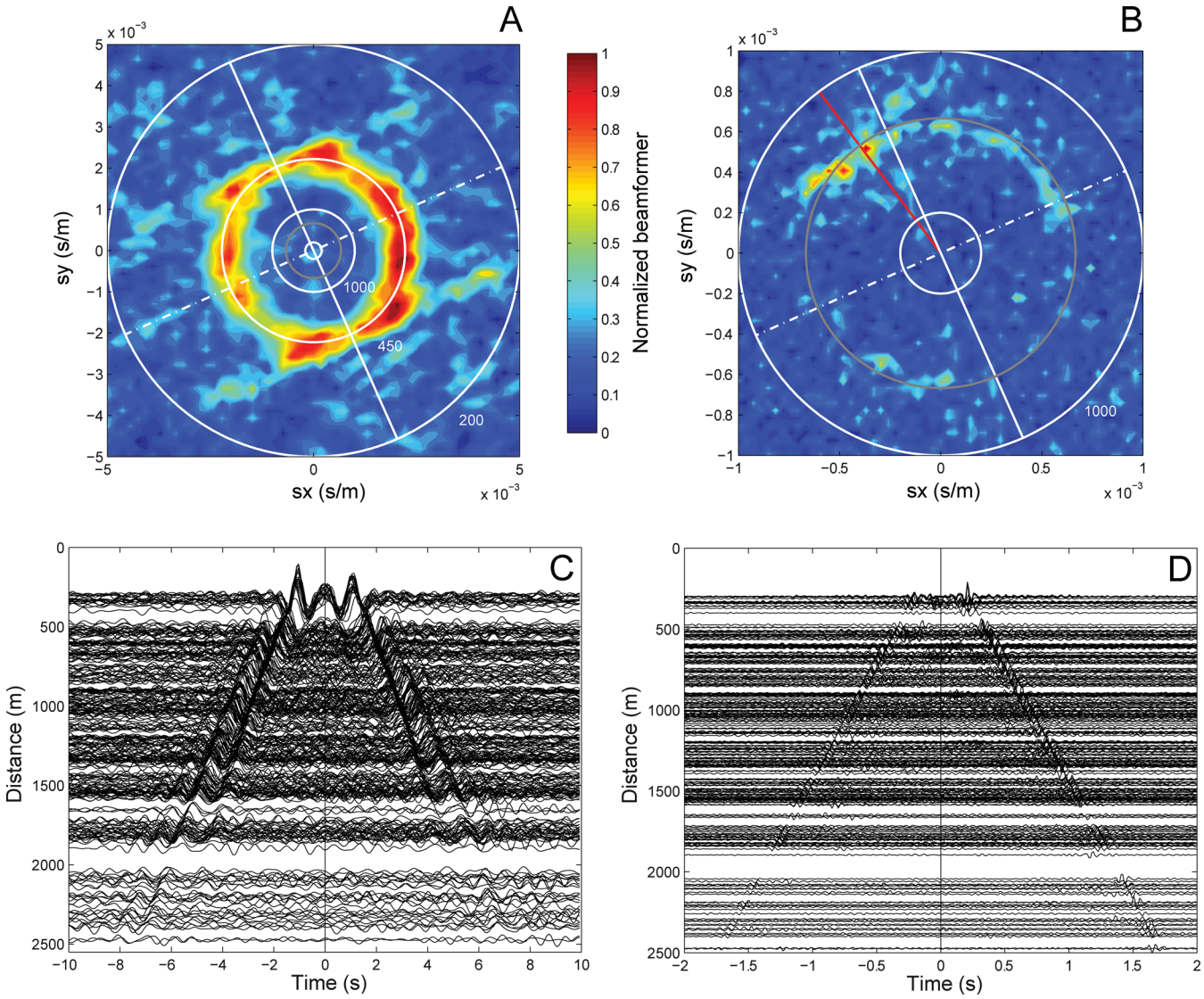

Figure 5. Results of the beamforming for the frequency bands 0.4–2 Hz (a) and 10–30 Hz (b). For reference, some constant phase velocities are shown with white circles. The grey circle represents the particular velocity of 1500 m s^{-1}. The solid white line shows the preferential azimuth along the cables of the *LoFS* array (155°) and the dotted one its perpendicular. The red line indicates the approximate direction of the platform. (c) ZZ Correlation functions between stations of the SR5 array filtered between 0.4 and 2 Hz and sorted by increasing interstation distance. A difference between the group and phase velocity is clearly seen. (d) same as (c) but filtered between 10 and 30 Hz. Note the different timescales.

noise-based group velocity tomography over the whole network. At higher frequencies, where the noise is mainly generated by the drilling platforms, we extracted and inverted surface waves propagating along a profile that is suitably oriented with respect to the localized noise source to produce a 2-D vertical *S*-wave velocity model.

4.1 Methods

We use Frequency Time Analysis (FTAN, Levshin *et al.* 1989) to measure group velocities from the computed noise CCs. Vertical-to-vertical geophone component CCs were used to make measurements for Scholte waves and transverse-to-transverse geophone component correlations for Love waves. We inverted the measured group velocities with the method of Barmin *et al.* (2001) that is based on ray theory with a Gaussian-shaped lateral smoothing. A group time t along a ray p can be computed as

$$t = \int_p \frac{\mathrm{d}s}{U(s)}, \tag{3}$$

where s is the distance along the ray and U is the group velocity. A traveltime perturbation δt relative to a reference velocity distribution U_0 is then expressed by

$$\delta t = t - t_0 = \int_p \frac{\mathrm{d}s}{U(s)} - \int_p \frac{\mathrm{d}s}{U_0(s)}. \tag{4}$$

Defining a model being $m = \frac{U_0 - U}{U}$, δt becomes a linear function of m. For the ith ray, we have

$$\delta_i t = G_i(m) = \int_{p_i} \frac{m}{U_0}\,\mathrm{d}s. \tag{5}$$

We assume that an observed traveltime is a sum of a real traveltime and an error ($t^{\mathrm{obs}} = t + \varepsilon$), and define a datum $d_i = \delta t_i^{\mathrm{obs}} = t_i^{\mathrm{obs}} - t_0$

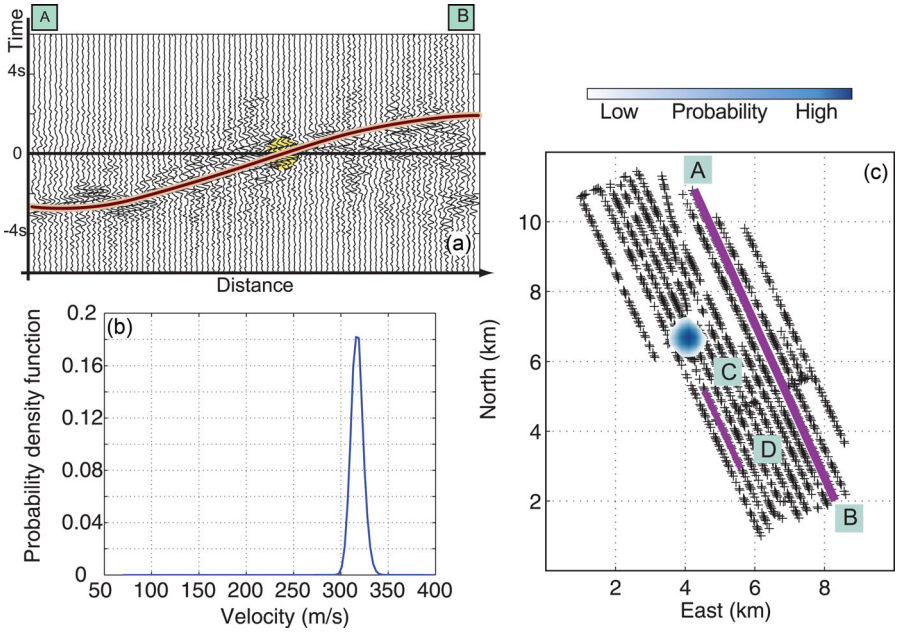

Figure 6. (a) ZZ Cross-correlations for pairs of stations separated by 500 m, located on the profile AB and low passed at 10 Hz. Brown line shows a cosine-like variation of traveltime indicating that the observed low-frequency waves are generated by a localized source. (b) Probability density of the average seismic velocity of the medium for the Love waves. (c) Probability density of the position of the high-frequency noise source of Love waves. The colour follows a logarithmic scale from high probability (blue) to null probability (white and transparent). The black crosses show the 1000 randomly chosen stations. Solid purple lines show profiles AB and CD shown in Figs 6(a) and 13, respectively.

where t_0 is the traveltime for a reference model (U_0). This results in

$$d_i = G_i(m) + \varepsilon_i. \tag{6}$$

To estimate m, we minimize the following penalty function:

$$S(m) = (G(m) - d)^\top C_\mathrm{d}^{-1}(G(m) - d) + \alpha \|F(m)\|^2 + \beta \|H(m)\|^2, \tag{7}$$

where m is the model, d is the data vector and G is the forward operator. C_d is the data covariance matrix, which we have assumed to be diagonal. The first term in eq. (7) represents the deviation of the model prediction from the data, the second term is the spatial smoothing condition and the third term is the damping constraint that penalizes the weighted norm of the model. A norm of an arbitrary function $f(r)$ can be defined as

$$\|f(r)\| = \int_S f^2(r)\,\mathrm{d}r. \tag{8}$$

The spatial smoothing term F involves a correlation length σ

$$F(m)(\mathbf{x}) = m(\mathbf{x}) - \int_S K(\mathbf{x}, \mathbf{x}')m(\mathbf{x}')\,\mathrm{d}\mathbf{x}' \tag{9}$$

with

$$K(\mathbf{x}, \mathbf{x}') = A \exp\left(-\frac{|\mathbf{x} - \mathbf{x}'|^2}{2\sigma^2}\right) \tag{10}$$

normalized such as $\int_S K(\mathbf{x}, \mathbf{x}')\,\mathrm{d}\mathbf{x}' = 1$.

The third term constrains the amplitude of the perturbations depending on local path density

$$H(m)(\mathbf{x}) = \exp(-\lambda\rho(\mathbf{x})), \tag{11}$$

where $\rho(\mathbf{x})$ is the path density around $\mathbf{x}$ and λ is a constant parameter. α, β, σ and λ are user-controlled parameters that are determined through systematic exploration of the misfit evolution with different realistic values of these parameters. The velocity distribution is discretized with a Cartesian grid where each cell has a constant velocity. Let N be the number of ray paths, $i = 1 \ldots N$, let M be the number of cells in the model, j, $k = 1 \ldots M$, then, $m(\mathbf{x}) = \mathbf{m}$ is an M-long vector containing the slowness for every cell and eq. (7) can be discretized and rewritten in matrix form

$$\mathbf{S(m)} = (\mathbf{Gm} - \mathbf{d})^\top \mathbf{C_d}^{-1}(\mathbf{Gm} - \mathbf{d}) + \mathbf{m}^\top \mathbf{Qm} \tag{12}$$

with

$$\mathbf{Q} = \alpha \mathbf{F}^\top \mathbf{F} + \beta \mathbf{H}^\top \mathbf{H}. \tag{13}$$

The matrix $\mathbf{G}$ is an $N \times M$ matrix containing the length of every path in every cell of the model

$$G_{ij} = \frac{l_{ij}}{U_{0_j}}, \tag{14}$$

where l_{ij} is the length of the ith path in the jth cell and U_{0_j} is the initial group velocity in the jth cell. The matrices $\mathbf{F}$ and $\mathbf{H}$ are $M \times M$ matrices and their components are defined by

$$F_{jk} = \delta_{jk} - \frac{K_{jk}}{\sum_k K_{jk}}, \tag{15}$$

where δ_{jk} is the Kronecker symbol and $K_{jk} = A \exp\left(-d_{jk}^2/2\sigma^2\right)$ with d_{jk} being the distance between the jth and kth cells.

$$H_{jk} = \exp(-\lambda\rho_j)\delta_{jk}, \tag{16}$$

where ρ_j is the number of paths crossing the jth cell.

With these definitions, the minimum of the function $\mathbf{S}$ is found at $\mathbf{m_{min}}$ with

$$\mathbf{m_{min}} = \mathbf{G}^* \mathbf{C_d}^{-1}\mathbf{d}, \tag{17}$$

where

$$\mathbf{G}^* = (\mathbf{G}^\top \mathbf{C_d}^{-1}\mathbf{G} + \mathbf{Q})^{-1}\mathbf{G}^\top. \tag{18}$$

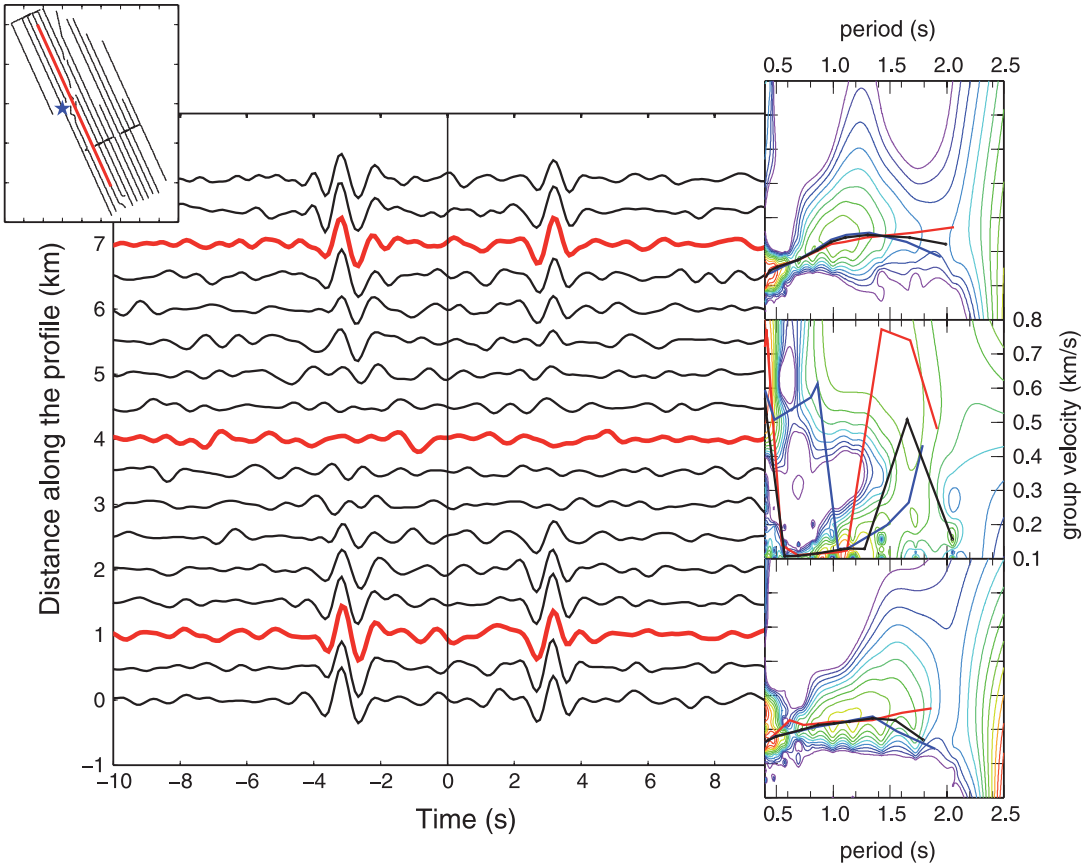

Figure 7. ZZ Noise cross-correlations computed between pairs of stations separated by ∼1 km and taken every 500 m along the profile shown in red on the inset (the star shows the platform position). CCs were filtered between 0.4 and 2 Hz. On the right side, examples of frequency–time diagrams and dispersion curves associated with the three CFs drawn in red are shown. The dispersion curves measured from the causal, the acausal and the symmetric parts are shown with the red, the blue and the black lines, respectively. Note the low signal-to-noise ratio on the CCs and the random behaviour of the dispersion curves near the platform.

We can also define the resolution matrix as

$$\mathbf{Res} = \mathbf{G}^{*}\mathbf{C_d}^{-1}\mathbf{G}. \quad (19)$$

We chose to use a strait ray theory tomography as a first-order approximation because of its implementation simplicity and the fairly good results it has showed in previous studies (e.g. Shapiro *et al.* 2005; Brenguier *et al.* 2007; Lin *et al.* 2008). Furthermore, the Gaussian rays should correct for most of deviations from this approximation.

4.2 Scholte wave tomography across the whole *LoFS* network

We used the vertical-to-vertical geophone component CCs filtered between 0.4 and 2 Hz to extract Scholte waves. We found that CCs for stations separated by more than 1.5 km had poor signal-to-noise ratio (SNR) whereas for interstation distances shorter than 1 km the signals from positive and negative lags of CCs are not well separated. This limit is similar to the three wavelengths minimal interstation threshold often used in the literature (e.g. Bensen *et al.* 2007). Therefore, we used only the station couples with interstation distances between 1 and 1.5 km. This selection resulted in ∼184 000 CCs, which represents about 7 per cent of the whole vertical-to-vertical data set and allows us to significantly reduce the computation time.

We further reduced the number of CCs by analysing the SNRs of the Scholte waves. The SNR was defined for the acausal and the causal sides of the CCs by the ratio between the maximum amplitude of each side and the standard deviation of the CC between −40 and −20 s and between 20 and 40 s, respectively. We found that the SNR of the CCs decreased dramatically close to the platform that leads to poor dispersion measurements. Fig. 7 shows 17 CCs computed for pairs of stations separated by 1 km located along a profile passing in the vicinity of the platform. We observe that the strong symmetrical signal around ±3 s disappears near the platform. This is because the continuous records are dominated by non-propagating platform-generated noise. Therefore, we chose to keep the CCs that had an SNR higher than 5 for both causal and acausal sides. The number of CCs kept by this procedure is summarized in Table 1.

We then measured group velocities from the causal, the acausal and the symmetric parts of the CCs (Fig. 8a). The group velocity differences between the causal and the acausal dispersion curves is used to evaluate the measurement quality. Indeed, we expect small differences between the dispersion curves from the causal and acausal sides for robust CC which has well converged to the GF.

The distributions of the number of measurements as a function of the group velocity difference showed a strong pick centred at 0 m s^{-1} difference indicating that most of the measurements were reliable (Fig. 8b). We defined the measurement errors for each frequency by the peak half-width at half-height of the distributions. Finally, we only inverted the dispersion curves measured from the symmetric parts of the CCs that resulted in causal–acausal group velocity

Table 1. Number of CCs fulfilling the different selection criteria.

	Frequencies								
	2.5 Hz	1.67 Hz	1.25 Hz	1 Hz	0.83 Hz	0.7 Hz	0.63 Hz	0.56 Hz	0.5 Hz
Initial # CCs	184 157	184 157	184 157	184 157	184 157	184 157	184 157	184 157	184 157
No. CCs SNR > 5	98 922	98 922	98 922	98 922	98 922	98 922	98 922	98 922	98 922
No. CCs P-N < 60 m s^{-1}	48 634	70 673	123 369	149 504	139 188	104 928	69 694	53 040	55 829
No. CCs for first step tomo.	27 130	43 869	80 715	97 059	93 676	72 368	45 894	30 991	34 967
No. CCs for second step tomo.	27 109	43 386	79 758	96 586	93 280	71 688	45 346	30 483	33 828
Per cent CCs used for tomo.	14.7 per cent	23.6 per cent	43.3 per cent	52.5 per cent	50.7 per cent	38.9 per cent	24.6 per cent	16.6 per cent	18.4 per cent

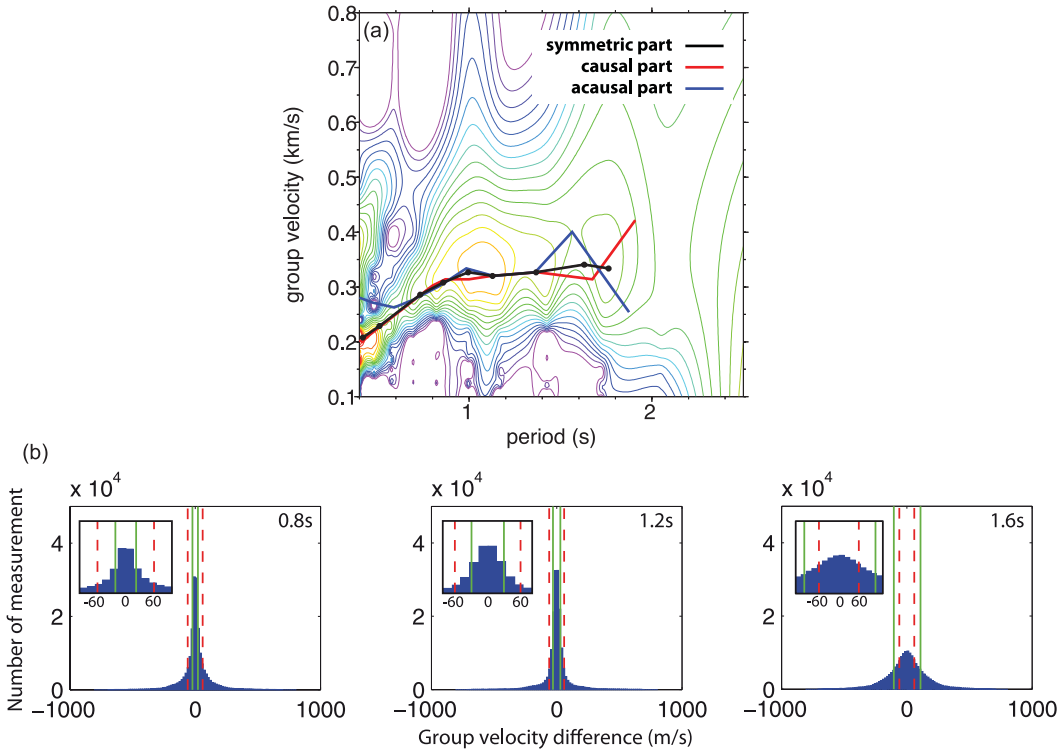

Figure 8. (a) Example of a frequency–time analysis (background of the figure) from the symmetric part of CC between receivers 1861 and 2063 (Fig. 1). Dispersion curves measured from the causal, acausal and symmetric parts are shown by red, blue and black curves, respectively. (b) Distributions of differences of group velocities measured from causal and acausal parts of CCs for three different periods: 0.8 s (1.25 Hz), 1.2 s (0.83 Hz) and 1.6 s (0.63 Hz). The green vertical lines denote the half-width at half-height of the distributions. The red dashed vertical lines denote the ±60 m s^{-1} range used for selection of dispersion measurements for the tomography.

differences smaller than 60 m s^{-1} for every periods (red dashed lines in Fig. 8b). It is aimed at eliminating most of low-quality dispersion measurements. Table 1 summarizes the number of CCs that were kept with this procedure for nine different frequencies between 0.4 and 2 Hz. Fig. 9 shows the paths that were kept by our selection procedure at 1.25 Hz. We can see that most of eliminated station pairs are within a 2-km-radius circle centred on the platform.

We inverted the selected measurements to compute for group velocity maps. Although we applied the tomography for the nine frequencies shown in Table 1, we present here results only for two frequencies: 0.83 and 1.25 Hz. The maps for the other frequencies are available as Supporting Information (Fig. S2). The results shown in this study are presented to illustrate the method and its accuracy, the interpretation of the full set of frequencies is out of the scope of this contribution. We used a grid composed of 90 × 115 square cells with a grid size of 100 m. The initial model had a constant velocity derived from the average of the mean and median group velocity for every period to account for extreme values of group velocity. We performed the inversion in two steps (Moschetti *et al.* 2007). First, we inverted a very smooth map that was used to identify and reject outliers (measurements with traveltime residuals greater than three standard deviations). The remaining measurements were used in the second step of tomography to yield the final high-resolution group velocity map. The traveltime residual was reduced significantly and the final results are robust. The ray coverage is very dense and homogeneous (Fig. 9). Fig. 10 shows the variance reduction as a function of the damping parameter values for all frequencies. We found that the damping parameter β and the coefficient λ had virtually no influence on the inversion and we set them set to 100 and 0.15, respectively, for every frequencies (Figs 10b–d). However, the choice of coefficients α and σ which control the smoothness affects strongly the final inversion results and the variance reduction. The damping factor α was set frequency-dependant (60 and 150 for 1.25 and 0.83 Hz, respectively, Fig. 10a) because the quality of the data was not constant along the data set and some frequencies needed a stronger smoothing to avoid the appearance of speckles. In general, we increase α for the frequencies which show a low variance reduction and decrease it for the frequencies with high

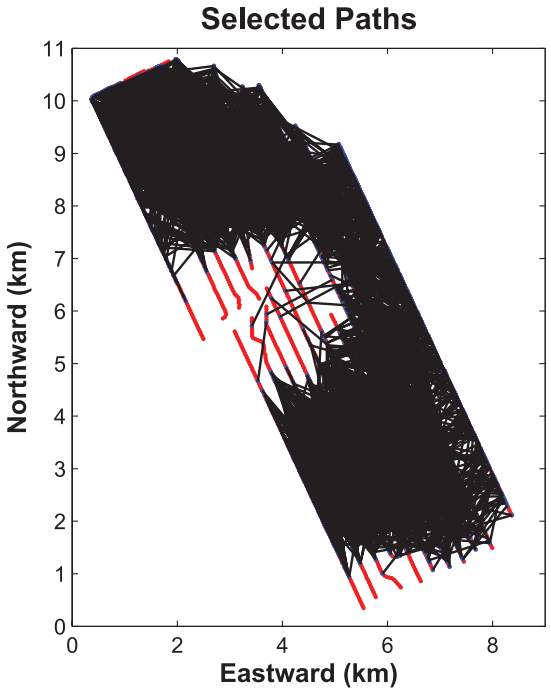

Figure 9. Interstation path coverage after the data selection at 1.25 Hz (0.8 s) (see Table 1 for details).

variance reduction (Fig. 10a). We did not chose the value of α and σ that leads to the minimum misfit (i.e. maximum variance reduction) because for these values the resulting velocity maps were strongly contaminated by small-scale patterns controlled by the stations and paths distribution. We chose a value of 80 m for σ for every frequencies using an L-curve criterion (Fig. 10c, Hansen & O'Leary 1993).

The final group velocity maps at 1.25 Hz (0.8 s) and 0.83 Hz (1.2 s) are shown in Figs 11 and 12, respectively. We show results for grid cells containing more than two rays. After applying different data selection criteria described above, we kept only from ∼14 per cent up to ∼50 per cent of paths for different frequencies. The amounts of data fulfilling each quality control step for every frequency are summarized in the Table 1. The path coverage in Figs 11(a) and 12(a) show that data quality control mainly rejected the data in the vicinity of platforms where the records were strongly contaminated by the platform-generated noise. Following Barmin *et al.* (2001), we computed resolution matrices at all nodes to estimate the spatial resolution of the group velocity maps. At every location, we fit a cone to the respective resolution map and take its radius as an estimation for the spatial resolution. We limit the minimal value of the spatial resolution to be twice the distance between two neighbour nodes, which is 200 m. Figs 11(b) and 12(b) show that the average resolution across the *LoFS* array is close to the main wavelength of the Scholte waves (300–500 m). While the resolution strongly degrades in the vicinity of the platforms, it

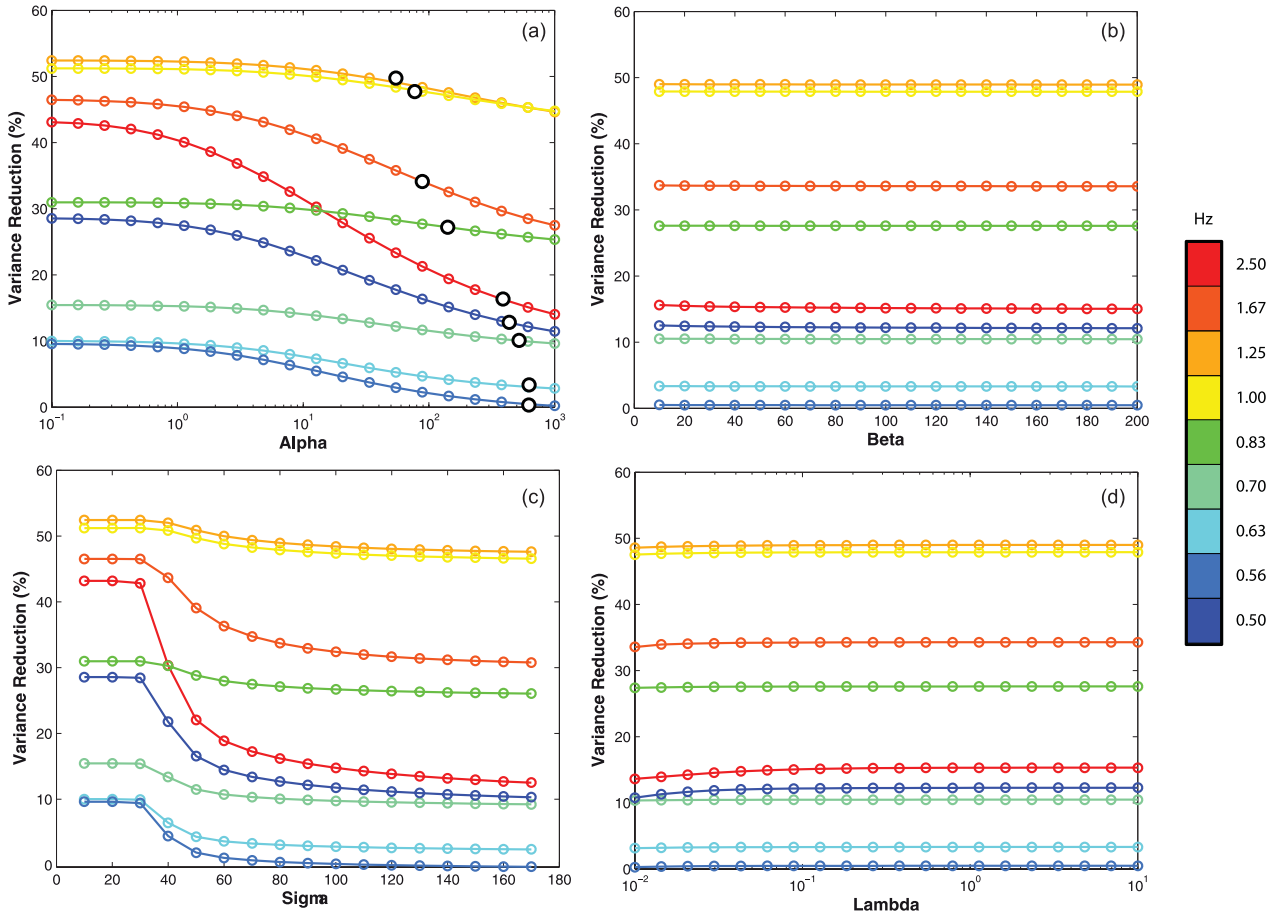

Figure 10. Variance reduction as function of the four different damping parameters and coefficients, α (frame a), β (frame b), σ (frame c) and λ (frame d), used for the tomography at all frequencies. The finally chosen values for the α parameter is circled in black for each frequency in frame (a).

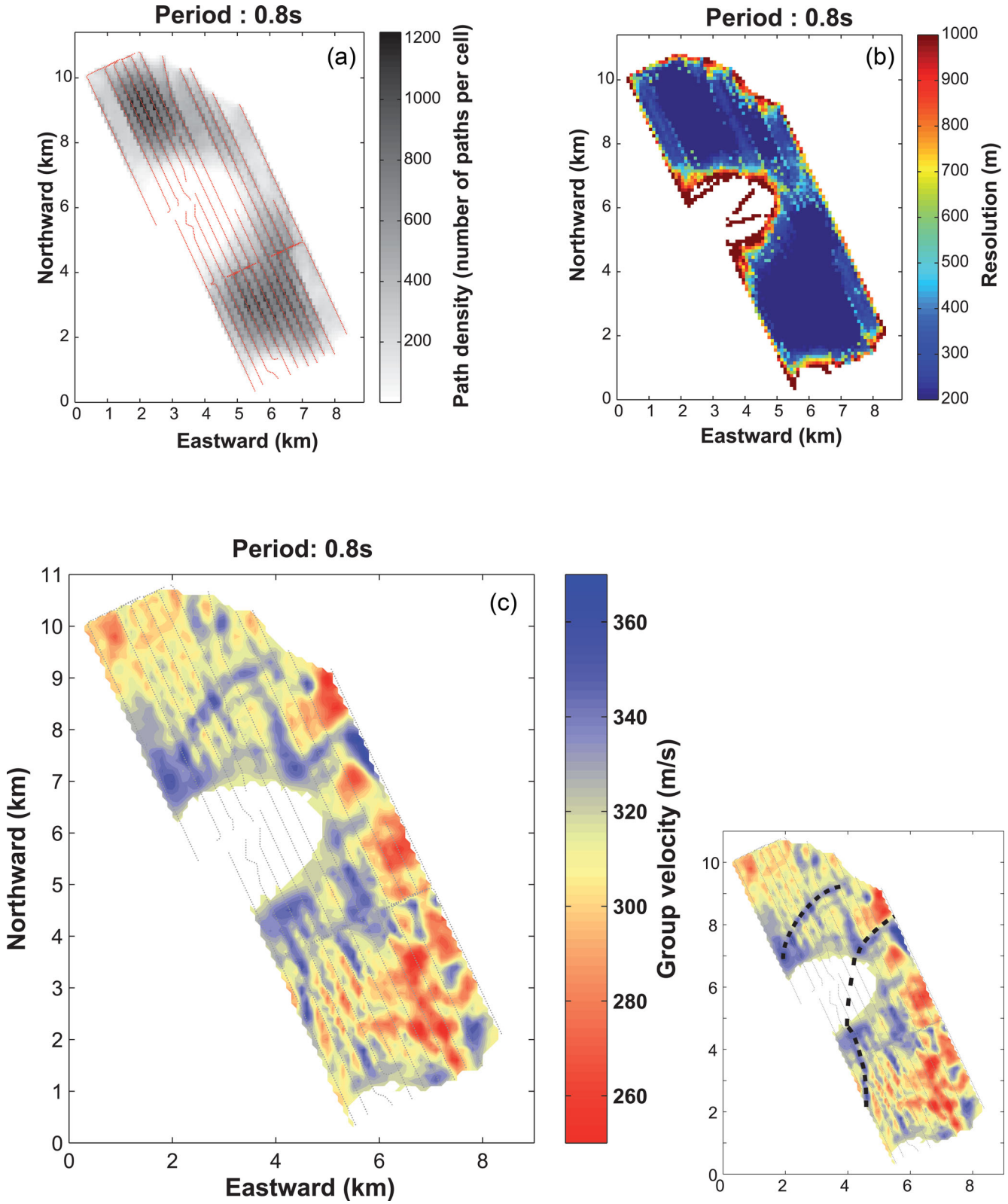

Figure 11. Results of the group velocity tomography inversion at 1.25 Hz (0.8 s). (a) Paths density map. (b) Spatial resolution map. (c) Scholte wave group velocity map. Dashed black lines on the tomography map are the interpretation of the shallow palaeochannels.

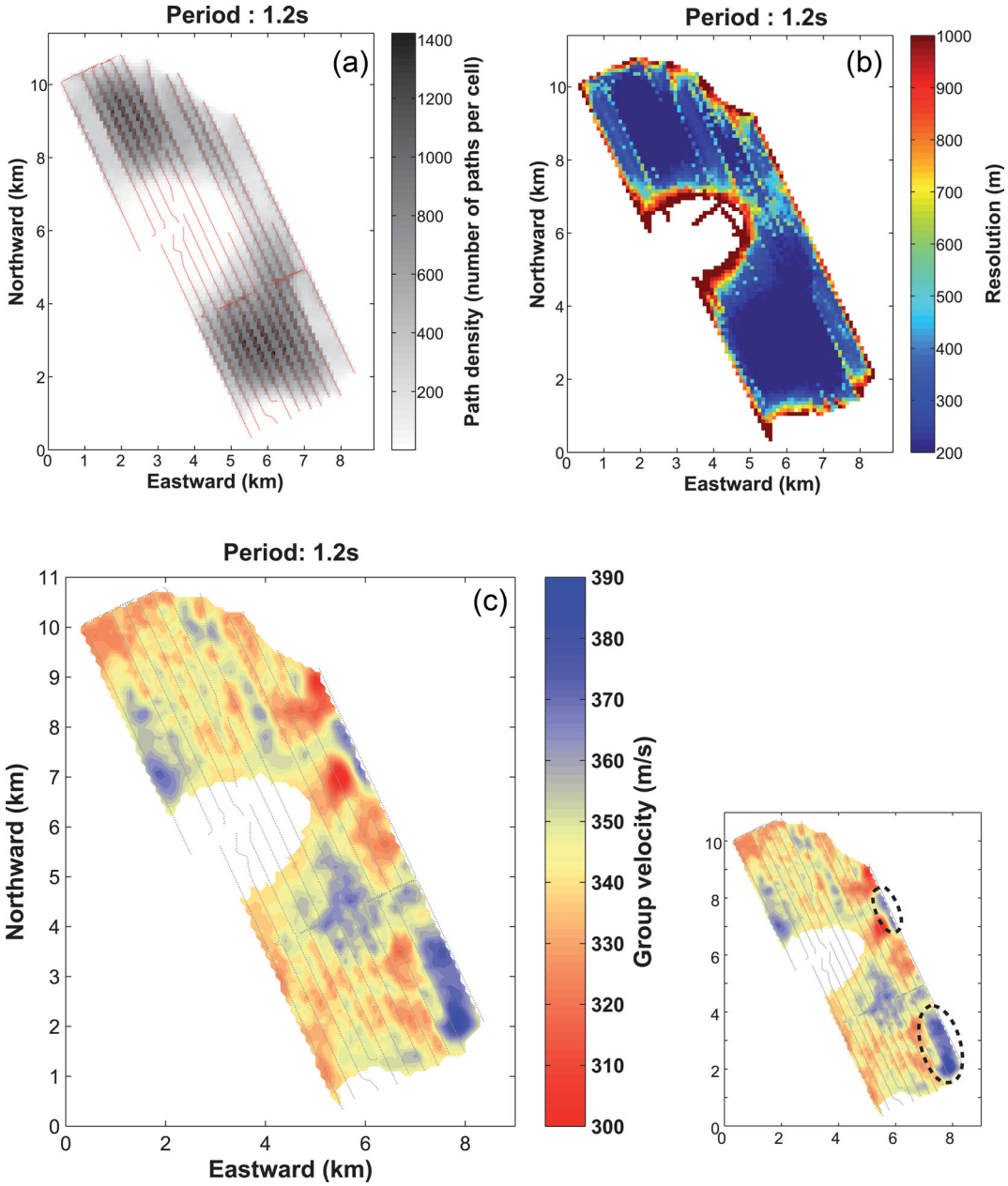

Figure 12. Results of the group velocity tomography inversion at 0.83 Hz (1.2 s). Notations are similar to Fig. 11. Dashed black ellipses on the tomography map highlight the large meandering deep palaeochannel.

approaches the maximum theoretical resolution in the areas with the best data coverage.

5 INVERSION ALONG A PROFILE AT HIGH FREQUENCIES

Since at frequencies above 2 Hz, the noise is mainly generated by the operating platforms (Fig. 6) that results in a very localized source distribution we decided to use this as a source and analyze the CCs along the profile CD (Fig. 13) because all considered pairs of stations are aligned in the direction of the dominant noise source. A preliminary analysis of these data demonstrated that the SNR is better at transverse-to-transverse CCs (Figs 13 and S3) that are associated with Love waves. A good estimation of the GFs for every receiver pair is obtained allowing us to perform a surface wave tomography along the profile. We measured dispersion for the Love waves for all 1225 interstation pairs of the profile and inverted frequency-dependent group velocities as a function of offset. Since a relatively broad range of frequencies were available, we were able to invert *S*-wave velocity as a function of depth.

5.1 Group velocity tomography

The analysis of the CCs showed that group velocities could be measured in two frequency bands: between 3 and 12 Hz and between 24 and 29 Hz with 1 Hz step. We did not retain the frequencies between 12 and 24 Hz because the data exhibited a significant spectral gap in this frequency band (Fig. S4). We performed a 1-D tomography along the profile CD with a grid spacing of 25 m. The spatial smoothing σ is set to 25 m for frequencies between 3 and 12 Hz

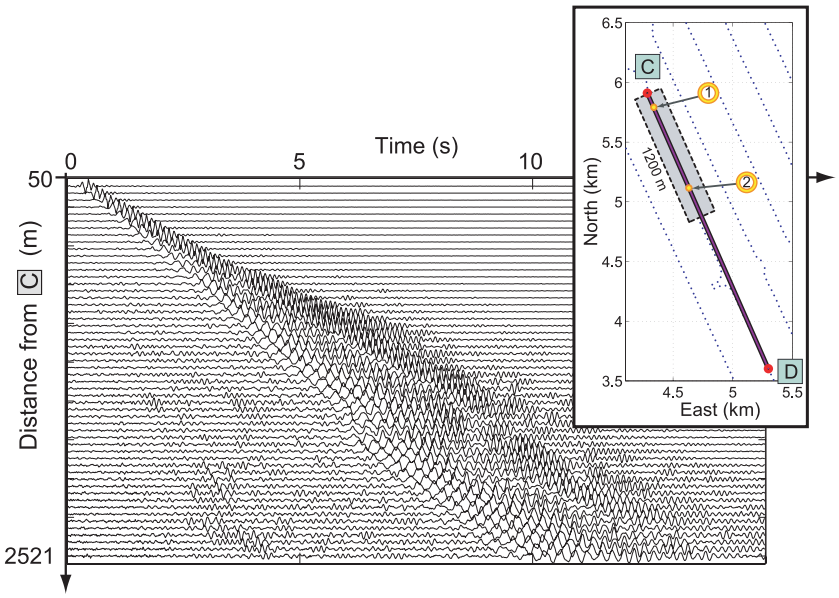

Figure 13. Transverse–transverse component CCs between all stations along the profile CD and the station located in C. Inset: Map of the profile CD. The rectangle delineates the resolved part of the profile used for the inversion in depth. The numbers 1 and 2 are the points inverted at depth shown in Fig. 16.

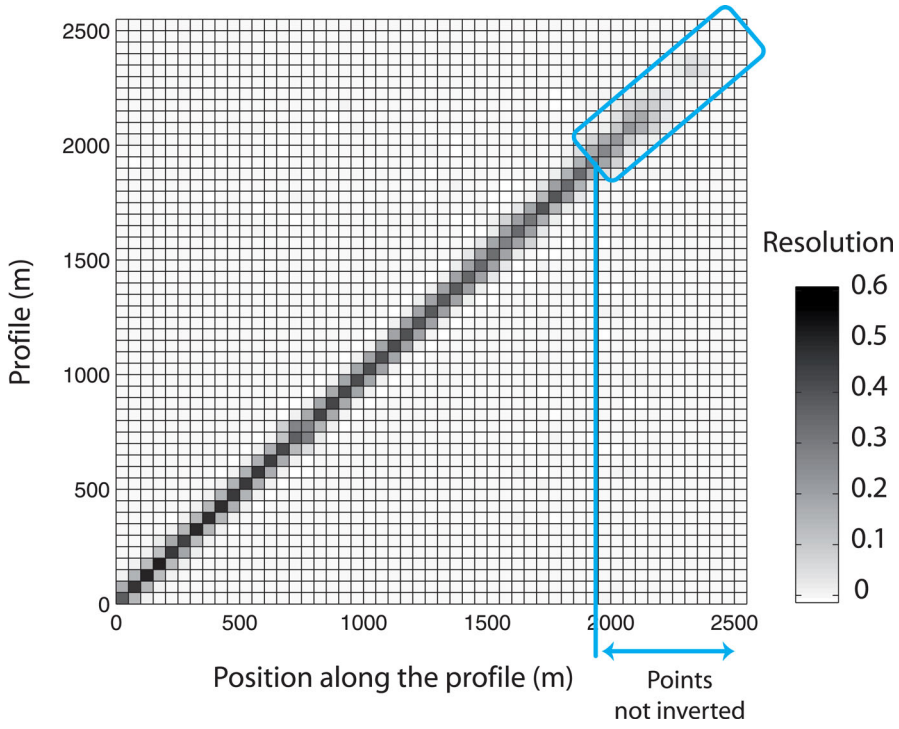

Figure 14. Resolution matrix for the tomographic inversion along the profile CD. Cells with resolution lower than 0.5 are discarded.

and 50 m between 24 and 29 Hz. The damping factor α is equal to 1 and β is set to 0 because the path density is homogeneous. When performing the tomography along a 1-D profile, the results of the resolution analysis for all points of the profile may be represented as a single square matrix where every column represents a resolution matrix for a single point (Fig. 14). In a case of a perfect model recovery, the only non-zero elements of this matrix will be equal to 1 and be on the diagonal. We use these diagonal values as a proxy for the quality of the inversion at a particular point and only retain results at locations where they are greater than 0.5. The group velocity distributions along the profile at different frequencies are shown in Fig. 15. First, from Fig. 15, we can see that the group velocities at high frequencies (24–29 Hz) are reasonably recovered at relatively short distances from the platform (less than 1250 m). Then, in Fig. 15, we observe a general decrease of the group velocities at most of frequencies towards the southern part of the profile, particularly a strong low-velocity anomaly near location (2). With a given group velocity in the ith cell, we introduce the uncertainty ΔV_i based on the diagonal terms of the resolution matrix r_i. We empirically fix $\Delta V_i = 15 \cdot (1 - r_i)$ in the 3–12 Hz frequency band and $\Delta V_i = 30 \cdot (1 - r_i)$ in 24–29 Hz. These values represent errors ranging from ~5 per cent to ~30 per cent of measurements.

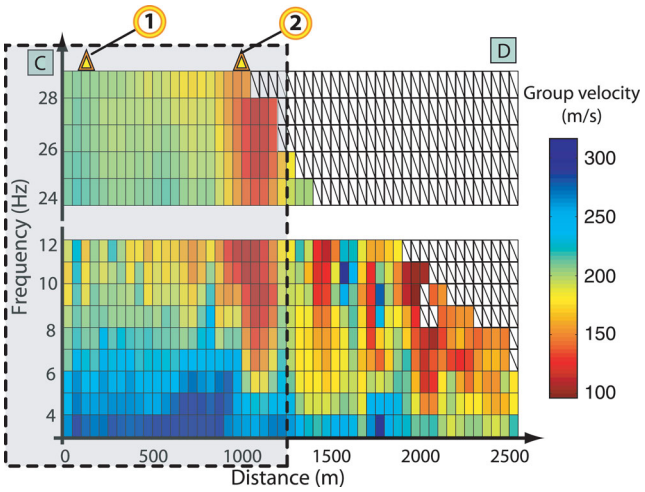

Figure 15. Results of Love wave group velocity inversion along the profile CD. White area indicates locations and frequencies where Love waves were not recovered. Dashed rectangle indicates the part of the profile that has been used for the depth inversion and static computation.

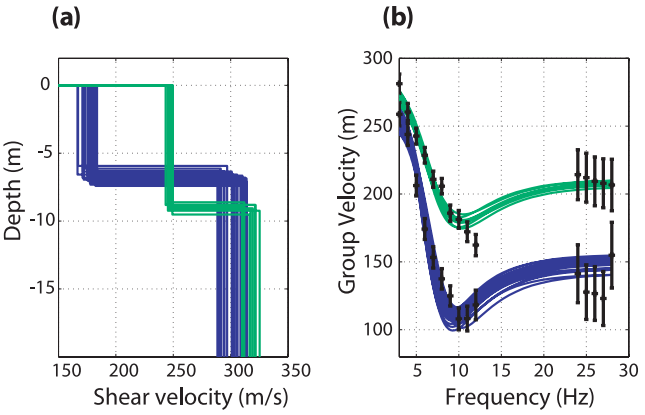

Figure 16. (a) Acceptable 1-D shear velocity models obtained with Monte Carlo inversions at locations 1 (blue lines) and 2 (green lines) indicated in Fig. 15. (b) Corresponding group velocity dispersion curves of Love waves. Black points with vertical error bars show group velocities estimated form the tomography and used as input data for the depth inversion.

5.2 Distribution of shear velocities with depth

For the part of the profile where the group velocities could be inverted at both high and low frequencies (dashed rectangle in Fig. 15), we inverted the dispersion curves to determine local 1-D *S*-wave velocity as a function of depth. For a small number of layers, we were able to sample the model space with a Monte Carlo approach (e.g. Shapiro *et al.* 1997).

After testing the inversion with different number of layers, we found that the dispersion data can constrain velocity down to 20 m. Therefore, we parametrized the model with a single layer over a half-space with only three unknowns: the thickness and the shear velocity in the top layer and the shear velocity in the half-space. A 70-m thick water layer is present above the model. Results of inversions at two locations are shown in Fig. 16. Even if the spectral gap might suggest the presence of the first overtone, we kept the modelling that invoked the simplest model, that is, the Love wave fundamental mode only, because it fits the dispersion curves reasonably. The shear velocity in the half-space do not vary strongly along the profile and main changes are found within the superficial layer (Fig. 15). It can be seen that both the thickness of the top layer and its shear velocity

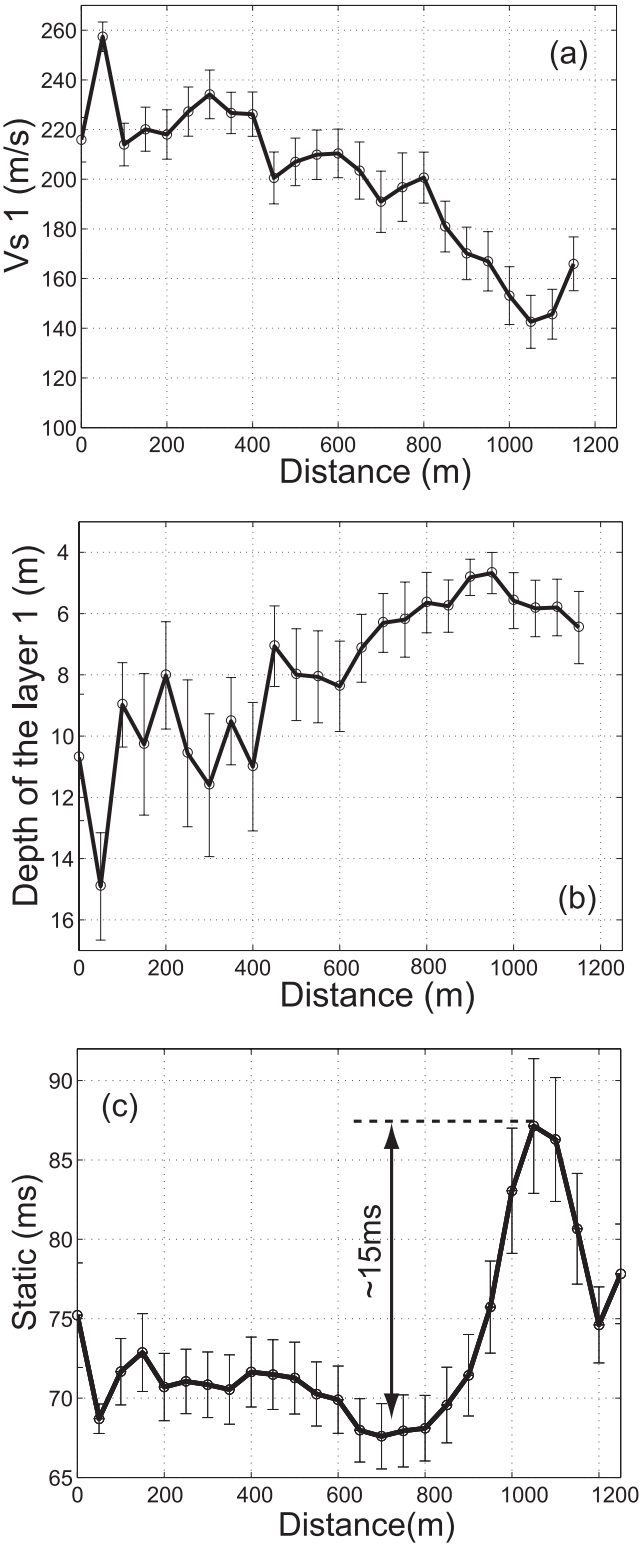

Figure 17. (a) Variations of the *S*-wave velocity of the first layer along the profile CD. (b) Variations of the depth of the first layer along the profile CD. (c) *S*-wave traveltime (average and standard deviation) computed in the top 20 m along the profile CD.

decrease with the distance from the platform (Figs 17a and b). There is a trade-off between these two parameters (velocity and depth) and therefore, we compute the traveltime that can be used for static correction. For every acceptable model, we calculated an

S-wave static in the top 20 m of the subsurface with the following equation:

$$Dt = \int_{0m}^{20m} \frac{\mathrm{d}z}{v(z)}. \quad (20)$$

Fig. 17(c) shows a particularly strong static (about 15 ms) near the location (2) where we measured lower than average group velocities (Fig. 15). This observation is important because such strong statics could damage *S*-wave image at depth.

6 DISCUSSION AND CONCLUSIONS

In agreement with previous study by de Ridder & Dellinger (2011), our results demonstrated that continuous 'noise' signals recorded in a shallow water marine environment at the Valhall field contain significant amount of coherent energy that can be exploited with the CC approach. First, we observe that in the microseismic band the noise sources are well distributed providing a good azimuthal coverage suitable for a surface wave tomography across the whole receiver network. We could measure Scholte waves and invert for group velocities at frequencies around 1 Hz which is the high-frequency limit of the secondary microseismic peak. At lower frequencies, we were limited by the sensitivity of the *LoFS* geophones and especially by the highpass filter applied to the data. At higher frequencies (above 2 Hz), the noise is dominated by sources generated by the operating platforms. Therefore, it was not possible to perform a broad-band surface wave tomography that allows estimation of *S*-wave velocity as a function of depth. However, high-frequency noise generated by the platform allowed the estimation of *S*-wave velocity along a 2-D profile.

If we assume that the depth of penetration of surface waves is approximately one-half or one-third of their wavelength, 1 Hz data would be sensitive down to ∼200 m below the seafloor. We compared our results with those obtained by Sirgue *et al.* (2010) from acoustic full-waveform inversion (FWI) of an active seismic data set and with an independent ambient noise tomography by de Ridder & Dellinger (2011). We found the presence of a set of narrow high-velocity anomalies on the 1.25 Hz (0.8 s) group velocity map (Fig. 11c) that were previously interpreted as buried palaeochannels (Sirgue *et al.* 2010; de Ridder & Dellinger 2011). We were also able to detect a larger meandering palaeochannel crossing the southeast corner of the *LoFS* array (Fig. 12c) that was not previously identified by de Ridder & Dellinger (2011). This feature is visible at frequencies lower than 0.83 Hz (1.2 s) indicating a deeper root which is in agreement with the FWI results. These palaeochannels appear as high-velocity anomalies because they are more likely to be filled with consolidated sand and gravels, media that exhibit velocities significantly higher than surrounding water-saturated sediments.

Results of our tomography maps confirm that the Valhall field subsurface has a complicated geological structure with many palaeogeomorphological features. The result obtained from the inversion along the profile CD (Fig. 15) can be interpreted as manifestation of these features. In particular, the strong low-velocity anomaly close to location (2) (Fig. 15) may be caused by a small palaeochannel filled with water-saturated and unconsolidated sediments. Moreover, the depth inversion along the profile shows that the depth of the superficial layer, as well as its velocity decrease when one get further from the platform (Figs 17b and c). This might be a signature of the strong seafloor subsidence beneath the platform due to the reservoir depletion caused by the oil exploitation (Hatchell *et al.* 2009). These observations correlate well with a contractional strain inside the subsidence bowl that would increase the seismic velocity. The same phenomenon may cause the general increase of seismic velocities towards the central part of the field that can be seen on group velocity maps at frequency higher than 1 Hz (Fig. 11). At lower frequencies, we observe the emergence of a low-velocity anomaly at the centre of the network (tomography maps from 1.6 to 2 s in Fig. S2). This effect may be explained by geotechnical models that consider extensional strain deeper in the subsurface, above the reservoir (e.g. Barkved & Kristiansen 2005; Barkved *et al.* 2005; Hatchell *et al.* 2009).

Our approach does not take into account the strong anisotropy present in the shallow subsurface (Barkved & Kristiansen 2005; Barkved *et al.* 2005; Hatchell *et al.* 2009). By doing so, we may limit the quality and the sharpness of our tomographic images and it may explain the relatively low variance reduction values obtained at frequency <1 Hz (Fig. 10). However, the overall results of our study remain qualitatively valid.

In this study, we used only a small part of the information that is contained in the full set of noise correlations between the receivers of the *LoFS* array. Our main objective here was to provide a study for a wide frequency range of the ambient noise surface wave tomography (ANSWT) in a marine environment for industry application. A more complete analyses of the whole data set (including all four-components of records) will be subject of future studies. It is interesting to note that we had 6.5 hr of data which was enough to extract waves propagating in superficial layers with high SNR from the noise CCs and to obtain high-resolution images of the subsurface. The quality and spatial resolution of the images could be improved with correlating noise records longer than 6 hr. In particular, this would help the signal reconstruction at high frequencies and in vicinity of the operating platforms. Recent studies of volcanoes and earthquakes (e.g. Sens-Schönfelder & Wegler 2006; Brenguier *et al.* 2008a,b; Clarke *et al.* 2011) indicate that noise tomography can be used as a monitoring tool by analysing the noise data on daily basis in the time-lapse mode. Therefore, it could also be possible to monitor changes in the elastic properties of the overburden in quasi-real time. Finally, an important improvement in the noise-based imaging and monitoring using OBC data would be recording of broad-band data that could help to extract signals at lower frequencies and fully explore the microseismic sources on the seafloor which would provide a better sensitivity to deeper parts of the subsurface.

Bussat & Kugler (2011) describe several potential application areas where ANSWT would be very useful and would help to overcome some issues arising with active seismic data. They cite, for instance, the possibility to better image subbasalt reservoirs and shallow salt structures. The surface waves extracted from the noise could also be used to measure anisotropy with a good accuracy. ANSWT could also add its contribution in FWI since one of its main problems is the absence of long-wavelength *S*-wave velocity. Most importantly, noise data are collected without any sources and at very low cost, hence ANSWT can be considered as a non-destructive and environmentally friendly method of seismic imaging. However, the surface wave tomography provides low-resolution image, which one has to reconcile with.

ACKNOWLEDGEMENTS

We thank BP Norge AS and the Valhall partner, Hess Norge AS, granting access to the seismic data. We thank Sjoerd de Ridder and

an anonymous reviewer for their constructive comments that help to improve the quality of this paper. This work of AM, ML, NS and PR was supported by an FP7 ERC Advanced grant 227507 (WHISPER). The IPGP contribution number is 3342.

REFERENCES

Barkved, O. & Kristiansen, T., 2005. Seismic time-lapse effects and stress changes: examples from a compacting reservoir, *Leading Edge,* **24,** 1244–1248.

Barkved, O., Heavey, P., Kjelstadli, R., Kleppan, T. & Kristiansen, T.G., 2003. Valhall Field—still on plateau after 20 years of production, in *Offshore Europe,* 2–5 September 2003, Aberdeen, United Kingdom, SPE 83957, 16pp.

Barkved, O., Kristiansen, T. & Fjær, E., 2005. The 4D seismic response of a compacting reservoir—examples from the Valhall Field, Norway, *SEG Technical Program Expanded Abstracts,* **24**(1), 2508–2511.

Barmin, M., Ritzwoller, M. & Levshin, A., 2001. A fast and reliable method for surface wave tomography, *Pure appl. Geophys.,* **158**(8), 1351–1375.

Bensen, G., Ritzwoller, M., Barmin, M., Levshin, A., Lin, F., Moschetti, M., Shapiro, N. & Yang, Y., 2007. Processing seismic ambient noise data to obtain reliable broad-band surface wave dispersion measurements, *Geophys. J. Int.,* **169**(3), 1239–1260.

Brenguier, F., Shapiro, N., Campillo, M., Nercessian, A. & Ferrazzini, V., 2007. 3-D surface wave tomography of the Piton de la Fournaise volcano using seismic noise correlations, *Geophys. Res. Lett.,* **34**(2), L02305.

Brenguier, F., Campillo, M., Hadziioannou, C., Shapiro, N., Nadeau, R. & Larose, E., 2008a. Postseismic relaxation along the San Andreas Fault at Parkfield from continuous seismological observations, *Science,* **321**(5895), 1478–1481.

Brenguier, F., Shapiro, N.M., Campillo, M., Ferrazzini, V., Duputel, Z., Coutant, O. & Nercessian, A., 2008b. Towards forecasting volcanic eruptions using seismic noise, *Nature Geosci.,* **1,** 128–130.

Bussat, S. & Kugler, S., 2011. Offshore ambient-noise surface-wave tomography above 0.1 Hz and its applications, *Leading Edge,* **30**(5), 514–524.

Campillo, M., Roux, P. & Shapiro, N.M., 2011. Using seismic noise to image and to monitor the Solid Earth, in *Encyclopedia of Solid Earth Geophysics,* ed. Gupta, Harsh K., pp. 1230–1235, Springer.

Clarke, D., Zaccarelli, L., Shapiro, N. & Brenguier, F., 2011. Assessment of resolution and accuracy of the moving window cross spectral technique for monitoring crustal temporal variations using ambient seismic noise, *Geophys. J. Int.,* **186,** 867–882.

de Ridder, S. & Dellinger, J., 2011. Ambient seismic noise eikonal tomography for near-surface imaging at Valhall, *Leading Edge,* **30,** 506–512.

Dellinger, J. & Yu, J., 2009. Low-frequency virtual point-source interferometry using conventional sensors, in *71st EAGE Conference and Exhibition*.

Duvall, T., Jefferies, S., Harvey, J. & Pomerantz, M., 1993. Time–distance helioseismology, *Nature,* **362,** 430–432.

Ekström, G., 2011. A global model of Love and Rayleigh surface wave dispersion and anisotropy, 25–250 s, *Geophys. J. Int.,* **187,** 1668–1686.

Gouédard, P. *et al.*, 2008. Cross-correlation of random fields: mathematical approach and applications, *Geophys. Prospect.,* **56**(3), 375–393.

Hansen, P. & O'Leary, D., 1993. The use of the L-Curve in the regularization of discrete ill-posed problems, *SIAM J. Sci. Comput.,* **14,** 1487–1503.

Harmon, N., Forsyth, D. & Webb, S., 2007. Using ambient seismic noise to determine short-period phase velocities and shallow shear velocities in young oceanic lithosphere, *Bull. seism. Soc. Am.,* **97**(6), 2009–2023.

Hatchell, P., Wills, P. & Didraga, C., 2009. Production induced effects on near-surface wave velocities at Valhall, in *71st EAGE Conference and Exhibition*.

Kimman, W. & Trampert, J., 2010. Approximations in seismic interferometry and their effects on surface waves, *Geophys. J. Int.,* **182**(1), 461–476.

Landès, M., Shapiro, N.M., Singh, S. & Johnston, R., 2009. Studying shallow seafloor structure based on correlations of continuous seismic records, *SEG Technical Program Expanded Abstracts,* **28**(1), 1693–1697.

Landès, M., Hubans, F., Shapiro, N., Paul, A. & Campillo, M., 2010. Origin of deep ocean microseisms by using teleseismic body waves, *J. geophys. Res.,* **115,** B05302, doi:10.1029/2009JB006918.

Levshin, A., Yanovskaya, T., Lander, A., Bukchin, B., Barmin, M., Ratnikova, L. & Its, E., 1989. *Seismic Surface Waves in a Laterally Inhomogeneous Earth,* Kluwer, Dordrecht.

Lin, F., Ritzwoller, M.H. & Shapiro, N.M., 2006. Is ambient noise tomography across ocean basins possible? *Geophys. Res. Lett.,* **33,** L14304, doi:10.1029/2006GL026610.

Lin, F., Ritzwoller, M., Townend, J., Bannister, S. & Savage, M., 2007. Ambient noise Rayleigh wave tomography of New Zealand, *Geophys. J. Int.,* **170**(2), 649–666.

Lin, F., Moschetti, M. & Ritzwoller, M., 2008. Surface wave tomography of the western United States from ambient seismic noise: Rayleigh and Love wave phase velocity maps, *Geophys. J. Int.,* **173**(1), 281–298.

Longuet-Higgins, M., 1950. A theory of the origin of microseisms, *Philos. Trans. R. Soc. Lond., A.,* **243**(857), 1–35.

Moschetti, M., Ritzwoller, M. & Shapiro, N., 2007. Surface wave tomography of the western United States from ambient seismic noise: Rayleigh wave group velocity maps, *Geochem. Geophys. Geosyst,* **8,** Q08010, doi:10.1029/2007GC001655.

Muyzert, E., Kommedal, J., Iranpour, K. & Olofsson, B., 2002. Near surface S-velocities, statics, and anisotropy estimated from Scholte waves, in *64th Annual Conference and Exhibition, EAGE,* Extended Abstracts, F, Vol. 28.

Ritzwoller, M. & Levshin, A., 1998. Eurasian surface wave tomography: group velocities, *J. geophys. Res.,* **103**(B3), 4839–4878.

Ritzwoller, M., Shapiro, N., Levshin, A. & Leahy, G., 2001. Crustal and upper mantle structure beneath Antarctica and surrounding oceans, *J. geophys. Res.,* **106**(12), 30645–30670.

Rost, S. & Thomas, C., 2002. Array seismology: methods and applications, *Rev. Geophys.,* **40**(3), 1008, doi:10.1029/2000RG000100.

Roux, P., 2009. Passive seismic imaging with directive ambient noise: application to surface waves and the San Andreas Fault in Parkfield, CA, *Geophys. J. Int.,* **179**(1), 367–373.

Sabra, K., Gerstoft, P., Roux, P., Kuperman, W. & Fehler, M., 2005. Surface wave tomography from microseisms in Southern California, *Geophys. Res. Lett.,* **32,** L14311, doi:10.1029/2005GL023155.

Sens-Schönfelder, C. & Wegler, U., 2006. Passive image interferometry and seasonal variations of seismic velocities at Merapi Volcano, Indonesia, *Geophys. Res. Lett.,* **33,** 1–5.

Shapiro, N. & Campillo, M., 2004. Emergence of broadband Rayleigh waves from correlations of the ambient seismic noise, *Geophys. Res. Lett,* **31**(7), doi:10.1029/2004GL019491.

Shapiro, N. & Ritzwoller, M., 2002. Monte-Carlo inversion for a global shear-velocity model of the crust and upper mantle, *Geophys. J. Int.,* **151**(1), 88–105.

Shapiro, N., Campillo, M., Paul, A., Singh, S., Jongmans, D. & Sánchez-Sesma, F., 1997. Surface-wave propagation across the Mexican volcanic belt and the origin of the long-period seismic-wave amplification in the valley of Mexico, *Geophys. J. Int.,* **128**(1), 151–166.

Shapiro, N., Campillo, M., Stehly, L. & Ritzwoller, M., 2005. High-resolution surface-wave tomography from ambient seismic noise, *Science,* **307**(5715), 1615–1618.

Shapiro, N., Ritzwoller, M. & Bensen, G., 2006. Source location of the 26 sec microseism from cross-correlations of ambient seismic noise, *Geophys. Res. Lett,* **33**.

Sirgue, L., Barkved, O., Dellinger, J., Etgen, J., Albertin, U. & Kommedal, J., 2010. Full waveform inversion: the next leap forward in imaging at Valhall, *First Break,* **28,** 65–70.

Snieder, R., 2004. Extracting the Green's function from the correlation of coda waves: a derivation based on stationary phase, *Physical Review E,* **69**(4), 46610, doi:10.1103/PhysRevE.69.046610.

Stehly, L., Campillo, M. & Shapiro, N., 2006. A study of the seismic noise from its long-range correlation properties, *J. geophys. Res.,* **111,** B10306, doi:10.1029/2005JB004237.

Stehly, L., Fry, B., Campillo, M., Shapiro, N., Guilbert, J., Boschi, L. & Giardini, D., 2009. Tomography of the Alpine region from observations of seismic ambient noise, *Geophys. J. Int.,* **178**(1), 338–350.

Stewart, P., 2006. Interferometric imaging of ocean bottom noise, in *2006 SEG Annual Meeting*.

Trampert, J. & Woodhouse, J., 1995. Global phase velocity maps of Love and Rayleigh waves between 40 and 150 seconds, *Geophys. J. Int.,* **122**(2), 675–690.

Trampert, J. & Woodhouse, J., 2003. Global anisotropic phase velocity maps for fundamental mode surface waves between 40 and 150 s, *Geophys. J. Int.,* **154**(1), 154–165.

van Gestel, J.-P., Kommedal, J.H., Barkved, O.I., Mundal, I., Bakke, R. & Best, K.D., 2008. Continuous seismic surveillance of Valhall Field, *Leading Edge,* **27**(12), 1616–1621.

Wapenaar, K., 2004. Retrieving the elastodynamic Green's function of an arbitrary inhomogeneous medium by cross correlation, *Phys. Rev. Lett.,* **93**(25), 254301, doi:10.1103/PhysRevLett.93.254301.

Weaver, R. & Lobkis, O., 2001. Ultrasonics without a source: thermal fluctuation correlations at MHz frequencies, *Phys. Rev. Lett.,* **87**(13), 134301, doi:10.1103/PhysRevLett.87.134301.

Webb, S., 1998. Broadband seismology and noise under the ocean, *Rev. Geophys.,* **36**(1), 105–142.

Yang, Y. & Ritzwoller, M., 2008. Characteristics of ambient seismic noise as a source for surface wave tomography, *Geochem. Geophys. Geosyst.,* **9**(2), Q02008, doi:10.1029/2007GC001814.

Yang, Y., Ritzwoller, M., Levshin, A. & Shapiro, N., 2007. Ambient noise Rayleigh wave tomography across Europe, *Geophys. J. Int.,* **168,** 259–274.

Yao, H., Gouédard, P., Collins, J., McGuire, J. & van der Hilst, R., 2011. Structure of young East Pacific Rise lithosphere from ambient noise correlation analysis of fundamental-and higher-mode Scholte-Rayleigh waves, *C. R. Geosci.,* **343,** 571–583.

Zheng, S., Sun, X., Song, X., Yang, Y. & Ritzwoller, M., 2008. Surface wave tomography of China from ambient seismic noise correlation, *Geochem. Geophys. Geosyst.,* **9**(8), Q05020, doi:10.1029/2008GC001981.

SUPPORTING INFORMATION

Additional Supporting Information may be found in the online version of this article:

Figure S1. (top) Probability density of the position of the high frequency noise source of Scholte waves on vertical-vertical components CCs. The color follows a logarithmic scale from high probability (blue) to null probability (white and transparent). The black crosses show the 1000 randomly chosen stations. (bottom) Probability density of the average Scholte wave velocity of the medium. Note that the source location is identical to the Love waves whereas the mean seismic velocity is lower as expected for Scholte waves.

Figure S2. Results of Scholte wave tomography analysed at all frequencies.

Figure S3. Vertical-vertical component CCs between all-stations along the profile CD and the station located in C. Inset: Map of the profile CD. The rectangle delineates the resolved part of the profile used for the inversion in depth. The numbers 1 and 2 are the points inverted at depth shown in Figure 16.

Figure S4. Frequency-Time Analysis of a transverse-transverse component CC from profile CD showing the spectral gap between 12 and 24 Hz. (http://gji.oxfordjournals.org/lookup/suppl/doi:10.1093/gji/ggt061/-/DC1)

Please note: Oxford University Press are not responsible for the content or functionality of any supporting materials supplied by the authors. Any queries (other than missing material) should be directed to the corresponding author for the article.